Electronic Transport in Low-Angle Twisted Bilayer Graphene

by

Yuan Cao

B.S. Physics
University of Science and Technology of China, 2014

SUBMITTED TO THE DEPARTMENT OF ELECTRICAL ENGINEERING AND COMPUTER SCIENCE IN PARTIAL FULFILLMENT OF THE REQUIREMENTS FOR THE DEGREE OF

MASTER OF SCIENCE IN ELECTRICAL ENGINEERING
AT THE
MASSACHUSETTS INSTITUTE OF TECHNOLOGY

JUNE 2016

©2016 Massachusetts Institute of Technology. All rights reserved.

Signature of Author: Signature redacted
Department of Electrical Engineering
and Computer Science
May 18, 2016

Certified by: Signature redacted
Pablo Jarillo-Herrero
Associate Professor of Physics
Thesis Supervisor

Accepted by: Signature redacted
Leslie A. Kolodziejski
Professor of Electrical Engineering
Chair of the Committee on Graduate Students

MASSACHUSETTS INSTITUTE OF TECHNOLOGY
JUL 12 2016
LIBRARIES
ARCHIVES

Electronic Transport in Low-Angle Twisted Bilayer Graphene

by

Yuan Cao

Submitted to the Department of Electrical Engineering and Computer Science on
May 18, 2016 in Partial Fulfillment of the Requirements for the Degree of Master
of Science in Electrical Engineering

ABSTRACT

Graphene is a two-dimensional material with exotic electronic, optical and mechanical properties. By stacking two layers of graphene together with a small rotation angle between them, a superlattice of arbitrarily large size can be formed. The hybridization of the electronic states in the two layers can result in reduced Fermi velocity, van Hove singularities and a gapped band structure.

In this work, a novel tear-and-stack technique is developed to reliably produce twisted bilayer graphene with controlled angle, and electronic transport measurements of the resulting high-quality samples are performed and discussed. We discover novel insulating states that purely results from the moiŕe superlattice band structure. The magnetotransport properties of these insulating states are studied and indicate that these states have different structure with those in either graphene or AB-stacked bilayer graphene; it shows a non-monotonous change of Fermi surface area which agrees with theoretical calculations. The results point toward a new pathway for graphene-related physics and material research.

Thesis Supervisor: Pablo Jarillo-Herrero
Title: Associate Professor of Physics

Contents

Abstract 3

1 Introduction 7

2 Theories of TwBLG 11
- 2.1 Tight-binding description of graphene 11
- 2.2 Continuum model of TwBLG 13
- 2.3 Tight-binding model of TwBLG 15
  - 2.3.1 Commensurate and Incommensurate 15
  - 2.3.2 Tight-binding Modeled Band structure 16
- 2.4 Symmetry in TwBLG 18

3 Experiment Techniques 21
- 3.1 Sample Fabrication 21
  - 3.1.1 Exfoliation 21
  - 3.1.2 Dry Transfer Technique 22
  - 3.1.3 Tear&Stack Modification 23
  - 3.1.4 Patterning & Contacting 25
- 3.2 Measurement 26
  - 3.2.1 Dilution Refrigerator 26
  - 3.2.2 Lock-in measurement 27

4 Experiment Results and Discussions 29
- 4.1 Atomic Force Microscopy 29
- 4.2 Raman Spectroscopy 29
- 4.3 Insulating States & Temperature Dependence 31
- 4.4 Magnetotransport 34
  - 4.4.1 Hall Effect and Hall mobility 34
  - 4.4.2 Landau Levels and Degeneracy 35

4.4.3 Shubnikov-de Haas Oscillation and Cyclotron Mass 38
4.5 Electric Field Dependence 40

5 Summary **43**

Acknowledgment **45**

References **47**

Chapter 1

Introduction

Since its discovery in 2005, graphene has remained a hot topic in both physics research and applications in next-generation electronic devices, thanks to its unique properties and robustness as a one-atom thin material[1]. For condense matter physicist, its most important electronic property is the linear energy dispersion near its charge neutrality, *i.e.* $E = \hbar v_F |\boldsymbol{k}|$, where $v_F \approx 1 \times 10^6\,\mathrm{m\,s^{-1}}$ is the Fermi velocity in graphene.

In a few years since then a whole new family of two-dimensional materials have emerged. In this family, there are insulators such as hexagonal boron nitride (h-BN), semiconductors such as MoS_2, and even superconductors such as $NbSe_2$. Interesting and complicated physics can happen when different layers of these materials are stacked together[2]. Recently, interests among physicist have arisen on what will happen when two or more layers of such two-dimensional sheets are stacked together with a rotational lattice mismatch. Studies on graphene/h-BN heterostructure, for example, have been carried out by numerous research groups[3, 4]. In this system many novel physics have been revealed, including the first realization of the famous Hofstadter's butterfly in a condense matter system, as well as a new energy gap at the Dirac point of graphene due to the breaking of inversion symmetry. These properties are observed only at small twisting angles (<5°) between the graphene and the h-BN crystal, which imposes a considerable difficulty on the sample preparation technique.

In the mean time, twisted bilayer graphene (TwBLG) has been attracting more and more attentions. Despite its similarity to the graphene/h-BN heterostructure, there are several fundamental differences between them. Because the two layers have exactly the same lattice constant, there is in principle no limit on the superlattice size one can get by twisting one of the layers[1]. Furthermore, instead of having a heterostructure of a conductive graphene sheet put on insulating h-BN, both graphene layers are conductive and the electronic states can strongly hybridize between them in different ways depending on the twist angle. In a recent work in Jarillo-Herrero group, it is shown that the two layers can behave independently if the twist angle is large, despite the apparent close distance between them (0.34 nm)[5]. However, precise characterization of low-angle twisted bilayer graphene has been a challenge so far, and fabrication of high-quality samples with controlled twisted angle has yet to be accomplished[6, 7].

There has been numerous literature that theoretically predicts the low-energy electronic properties in TwBLG, most notably the reduced Fermi velocity and emergence of van Hove singularities[8, 9]. These effects are experimentally observed in Scanning Tunneling Microscopy/Spectroscopy (STM/STS) experiments[10, 11, 12, 13] and Angular Resolved Photo-Emission Spectroscopy (ARPES) experiments[14, 15].

In a few more recent theoretical papers, the band structure and Landau level spectrum of TwBLG are more systematically investigated using tight-binding calculations[17, 18]. A pair of energy gaps and satellite Landau fans associated with them are expected to show up at the full filling of the lowest-energy superlattice bands, when the twist angle is smaller than about 2°. These gaps should be detectable in a conventional magnetotransport study. Previous transport studies on TwBLG at low twist angles have observed the emergence of satellite Landau fans[7]. However, the Landau level spectrum from the experiment was elusive and no experimental evidence to date directly points towards the existence of the insulating states at the full filling of the superlattice bands.

In this study, effort is first made in developing a reliable way of making high-quality samples with arbitrarily controlled angle. The trick is to tear a single piece of graphene using another piece of h-BN, then stack the two halves together keeping their original orientations, and thus retaining the relative angle between their lattices. These high-quality samples are measured in low temperatures and high magnetic fields. The electronic properties and the band structure can then be deduced from the measurement data and compared with theoretical predictions.

This thesis is arranged as following. In Chapter 2, I will describe the model and band structure for describing the electronic properties of TwBLG. Chapter 3 describes the experimental techniques that are used for fabricating and measuring the devices. In Chapter 4 I will analyze the experimental data and compare it with theoretical predictions. Finally in Chapter 5 I will conclude this thesis by providing some future perspectives in this area of study.

---

[1] However, in reality the nature will not allow this to happen because of relaxation to AB-stacked bilayer graphene at very low twist angles.

Chapter 2

Theories of TwBLG

In this chapter, I will first briefly talk about the microscopic theory for the electronic properties of monolayer graphene, with which TwBLG is built up. Then I will introduce two different descriptions for a TwBLG: the continuum approximation and the tight-binding model. Despite its simpleness, the continuum model can give qualitatively correct dispersion and topology at low energies and predict the reduction of Fermi velocity and the existence of van Hove singularities. On the other hand, the tight-binding model considers all possible hopping terms between all atoms in a moife superlattice, thus providing a complete picture of the electronic structure in TwBLG.

2.1 Tight-binding description of graphene

Graphene is a two-dimensional honeycomb lattice consisting of carbon atoms. The unit cell of graphene has two equivalent atoms (usually named A and B) and form a hexagonal lattice [Fig. 2.1(a)]. Each carbon atom in this lattice assumes a sp^2 hybridization. The three in-plane orbits bond with adjacent atoms to form strong σ-bonds and the electrons in the p_z orbit can 'hop' in the entire plane through the π-bonds[19].

If we only consider the hopping between nearest sites, *i.e.* from A site to the adjacent B site or *vice versa*, the tight-binding Hamiltonian of graphene is written in the second-quantized form as

$$H = t \sum_{i,j=\langle i \rangle} a_i^\dagger b_j + \text{h.c.} \tag{2.1}$$

In this equation, a_i, $a_i^\dagger$ and b_i, $b_i^\dagger$ are the annihilation and creation operators on the A and B sites respectively. $t \approx -2.7\,\mathrm{eV}$ is the nearest hopping energy. The diagonalization of this tight-binding Hamiltonian is straightforward. By doing replacement

$$a_i^\dagger = \sum_{\boldsymbol{k}} e^{i\boldsymbol{k}\cdot\boldsymbol{r}_{i,A}} a_{\boldsymbol{k}}, \qquad b_i^\dagger = \sum_{\boldsymbol{k}} e^{i\boldsymbol{k}\cdot\boldsymbol{r}_{i,B}} b_{\boldsymbol{k}}, \tag{2.2}$$

the Hamiltonian is block diagonal in $\boldsymbol{k}$-space representation.

$$H = \sum_{\boldsymbol{k}} H(\boldsymbol{k}) = \sum_{\boldsymbol{k}} f(\boldsymbol{k}) a_{\boldsymbol{k}}^\dagger b_{\boldsymbol{k}} + \text{h.c.} \tag{2.3}$$

$f(\boldsymbol{k}) = \sum_{j=1}^{3} \exp\left(i\boldsymbol{k}\cdot\boldsymbol{\delta}_j\right)$ sums over all three possible hopping paths from B site to adjacent A sites. The eigenvalues of the Hamiltonian *i.e.* the energy dispersion in $\boldsymbol{k}$ space can be solved to be

$$E_{\pm}(\boldsymbol{k}) = \pm|f(\boldsymbol{k})|. \tag{2.4}$$

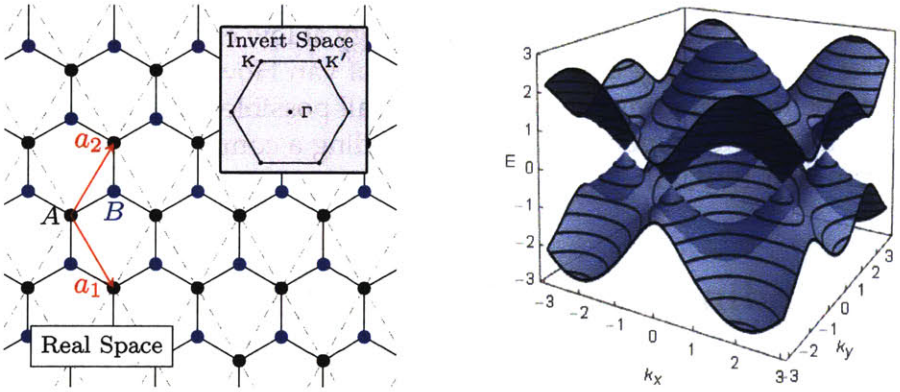

(a) Atomic Structure (b) Energy Dispersion

Figure 2.1: Monolayer Graphene

This energy dispersion is plotted in Figure 2.1(b). As can be seen in the plot, the two bands touch at the K and K' corners of the first Brillouin zone. If we expand the Hamiltonian near one of the two corners (or *valleys* as are usually called), we obtain a massless Dirac Hamiltonian that describes a two-level system with inversion symmetry. For example, near the K valley we have

$$H(\boldsymbol{K}+\boldsymbol{q}) \approx \hbar v_F \begin{bmatrix} 0 & q_x - iq_y \\ q_x + iq_y & 0 \end{bmatrix} = \hbar v_F \boldsymbol{\sigma}\cdot\boldsymbol{q}. \tag{2.5}$$

Here we have represented the operators on the two sublattices A and B in a two-component spinor form, and $v_F = 3ta/2$ is the effective Fermi velocity in graphene.

These equations hold as the basis for analyzing composite graphene systems such as a TwBLG. Although we have only considered the nearest-neighbor hopping here, it can be in general proved that as long as the A/B sublattice symmetry in graphene is preserved, this massless Dirac dispersion will be retained at low energies, and gap-opening is generally not allowed at the Dirac points.

2.2 Continuum model of TwBLG

When two layers of graphene are stacked together closely in real space, the easiest way to understand the composite system is to treat the atoms on each layer as perturbations to the electrons on the other layer. In this treatment we use the plane-wave in each layer as basis for constructing a perturbed Hamiltonian.

Instead of acting on a two-component spinor $[a_k, b_k]^T$ as in the case of graphene, the continuum model Hamiltonian of TwBLG acts on a four-component spinor $[a_k^{(1)}, b_k^{(1)}, a_k^{(2)}, b_k^{(2)}]^T$ accounting for the two layers and has a form of[8, 9, 20]

$$H(\boldsymbol{k}) = \begin{bmatrix} \hbar v_F \boldsymbol{\sigma} \cdot (\boldsymbol{k} - \boldsymbol{K}^{(1)}) & H_\perp \\ H_\perp^\dagger & \hbar v_F \boldsymbol{\sigma} \cdot (\boldsymbol{k} - \boldsymbol{K}^{(2)}) \end{bmatrix}. \tag{2.6}$$

The diagonal sub-matrices describe the intra-layer dispersion of each graphene layer and the four elements in $H_\perp$ denote the inter-layer coupling between $a_k^{(1)}, b_k^{(1)}$ and $a_k^{(2)}, b_k^{(2)}$ respectively.

In the zeroth order approximation, the inter-layer coupling is treated as uniform across the unit cell. In the limit of low twist angles, $H_\perp$ is usually assumed to be the same as in AB bilayer graphene, that can be written as

$$H_\perp = t_\perp \begin{bmatrix} 0 & 0 \\ 1 & 0 \end{bmatrix}, \tag{2.7}$$

which means that only B sublattice on layer 1 couples to A sublattice on the layer 2.

Similar to a AB bilayer graphene problem, one can approximate the 4-component spinor with a 2-component spinor that only describes B1 and A2 sublattices when considering the low-energy behaviors. This projection of Eq.(2.7) yields an effective Hamiltonian that reads

$$H^{\text{eff}}(\boldsymbol{k}) = -\frac{\hbar^2 v_F^2}{t_\perp}\begin{bmatrix} 0 & (k_x - ik_y)^2 - (\Delta K_x - i\Delta K_y)^2/4 \\ (k_x + ik_y)^2 - (\Delta K_x + i\Delta K_y)^2/4 & 0 \end{bmatrix}. \tag{2.8}$$

$\Delta \boldsymbol{K} = \boldsymbol{K}^{(1)} - \boldsymbol{K}^{(2)}$. The effective Hamiltonian for a bilayer graphene is recovered when $\Delta \boldsymbol{K} \to \boldsymbol{0}$. Numerical solution of this Hamiltonian for an AB bilayer graphene and a TwBLG is shown in Fig. 2.2.

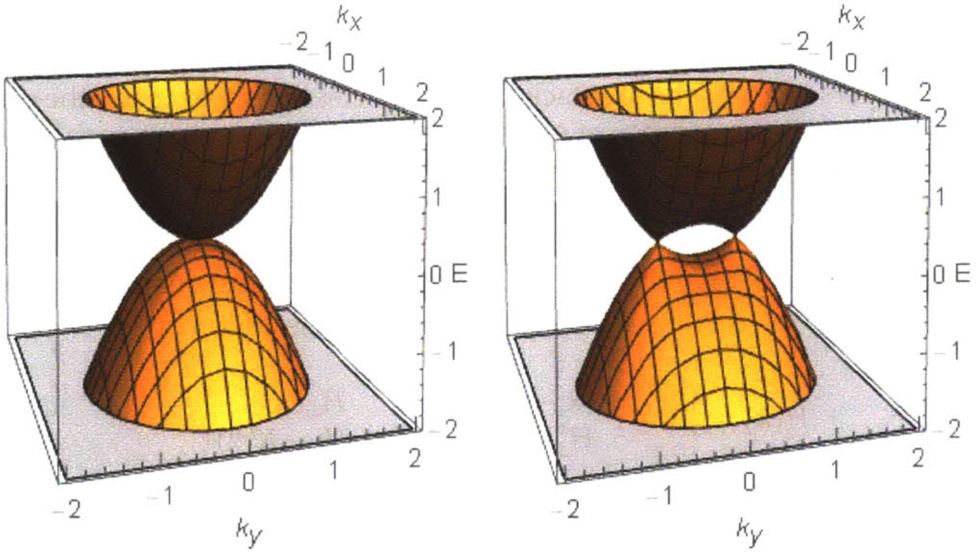

(a) AB bilayer graphene (b) TwBLG

Figure 2.2: Energy dispersion of bilayer graphene and TwBLG calculated with a continuum model.

This simple model captures several important low-energy features of the band structure of a TwBLG. As can be seen, the massless Dirac dispersion is retained at each of the original Dirac points of the two layers respectively, despite a reduction in the Fermi velocity. It can be analytically derived that this reduction ratio is equal to

$$\frac{v(\Delta \boldsymbol{K})}{v_F} = 1 - \left(\frac{3t_\perp}{\hbar v_F \Delta K}\right)^2. \tag{2.9}$$

The model also shows a van Hove sinularity at $\boldsymbol{k} = \boldsymbol{0}$, *i.e.* at the middle point between $K^{(1)}$ and $K^{(2)}$. However, this effective low-energy theory does not apply at high energies far away from the Dirac points. It also does not include any effects from the moiŕe superlattice that is essential in understanding a small angle TwBLG. These effects can be accounted for by including more Fourier components in the $H_\perp$ matrix.

2.3 Tight-binding model of TwBLG

As we see in the last section, the simple continuum model does not provide us enough information for a thorough understanding of TwBLG. A more realistic and complete model is needed to describe the microscopic behavior of a TwBLG. Similar to graphene, a TwBLG can be well approximated by a tight-binding model with the exception that we now need to consider the inter-layer σ-bonds between p_z orbits.

Before we construct the tight-binding model for TwBLG, we first introduce the concept of commensuration and build a mathematical description of the unit cell of a TwBLG.

2.3.1 Commensurate and Incommensurate

When two lattices are stacked together with a relative twist, there is in general no strict spatial periodicity in the resulting structure except for some special cases. Whenever there is such a periodicity, this composite structure is *commensurate*, otherwise *incommensurate*. Examples of the two situations are shown in Fig. 2.3. The usual notation for describing a commensurate structure is to use a pair of integers (n, m) such that the lattice vectors of the superlattice can be written as

$$\boldsymbol{A}_1 = n\boldsymbol{a}_1 + m\boldsymbol{a}_2, \tag{2.10}$$

$$\boldsymbol{A}_2 = -m\boldsymbol{a}_1 + (n+m)\boldsymbol{a}_2. \tag{2.11}$$

$\boldsymbol{a}_1$ and $\boldsymbol{a}_2$ are the lattice vectors of *one* of the two layers.

Tight-binding model and the associated mini Brillouin zone (MBZ) is well-defined only for periodic lattices, *i.e.* commensurate structures. However in an experiment incommensurate structures can possibly be fabricated, especially when the twist angle is large. The behavior of such structures still remains a mystery so far. In this thesis, we will be mainly focusing on commensurate structures. Our experiment are performed on small angle TwBLG which we think incommensurate structures might relax into a nearby commensurate structure easily.

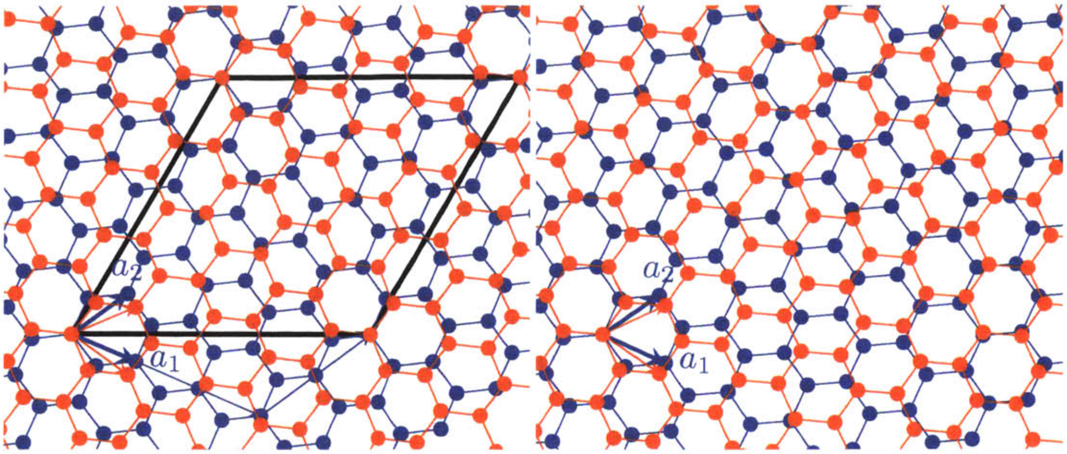

(a) Commensurate (3,2), $\theta = 13.17°$ (b) Incommensurate, $\theta = 5°$

Figure 2.3: Commensurate and Incommensurate TwBLG atomic structures.

The total number of atoms defined in such a commensurate unit cell is

$$N = 4(n^2 + m^2 + nm). \tag{2.12}$$

2.3.2 Tight-binding Modeled Band structure

With all the atoms positions in the unit cell known, we can now construct the $N \times N$ tight-binding Hamiltonian. Following the procedure described in Section 2.1, we can directly write it down as

$$\begin{aligned} H(\boldsymbol{k}) = & \sum_{\substack{i \in \text{layer1} \\ j = \langle i \rangle}} t(j) e^{i\boldsymbol{k}\cdot\delta_j} a^{(1)\dagger}_{\boldsymbol{k},i} a^{(1)}_{\boldsymbol{k},j} + \sum_{\substack{i \in \text{layer2,} \\ j = \langle i \rangle}} t(j) e^{i\boldsymbol{k}\cdot\delta_j} a^{(2)\dagger}_{\boldsymbol{k},i} a^{(2)}_{\boldsymbol{k},j} \\ & + \left(\sum_{\substack{i \in \text{layer1,} \\ j \in \text{layer2}}} t_\perp(i,j) e^{i\boldsymbol{k}\cdot(\boldsymbol{r}_i - \boldsymbol{r}_j)} a^{(1)\dagger}_{\boldsymbol{k},i} a^{(2)}_{\boldsymbol{k},j} + \text{h.c.} \right). \end{aligned} \tag{2.13}$$

In the first two summations i sums over all sites in a commensurate unit cell in one layer and j over all neighboring intra-layer hopping terms that are of interest. In the third summation i and j sum over all sites in opposite layers to account for possible inter-layer hopping terms.

The intra-layer hopping energies $t(j)$ are usually directly adapted from those used for graphene. However, it turns out that the choice of *inter-layer* hopping $t_\perp(i,j)$ makes a significant difference on the band structure, and this choice differs from literature to literature. In Ref.[17] for example, $t_\perp$ is chosen such that the resulting band structure matches the low-energy dispersion of bulk graphite. In Ref.[18] the parameters are fitted to DFT calculations of bilayer graphene and TwBLG with a small number of atoms in the unit cell.

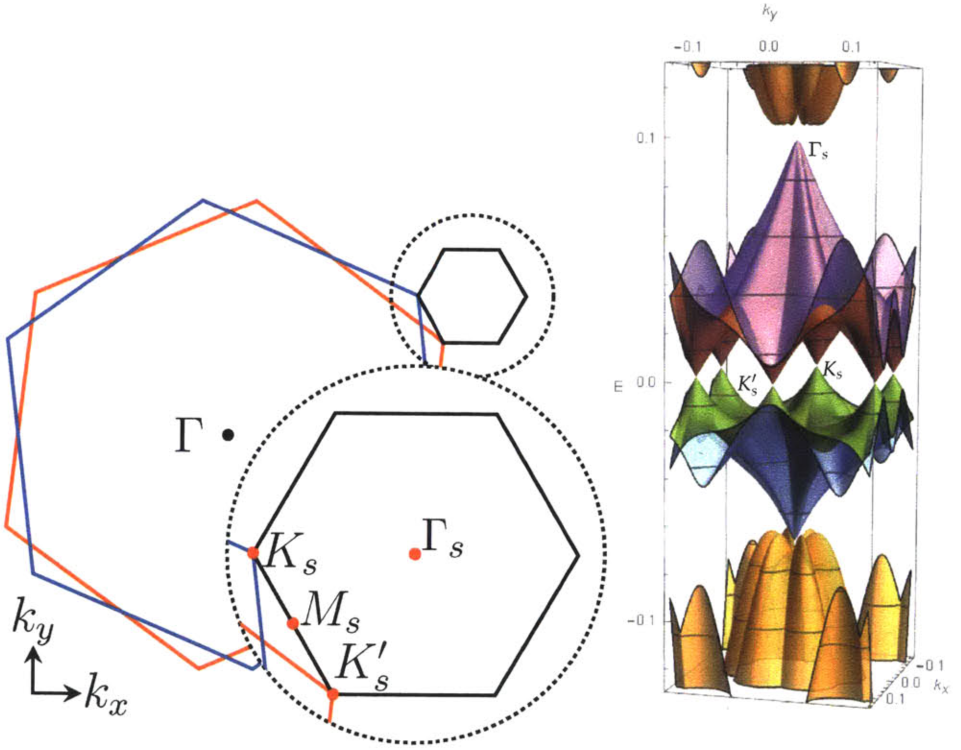

(a) Definition of mini Brillouin zone (exaggerated) (b) Tight-binding band structure

Figure 2.4: Illustration of MBZ that corresponds to a $(n, n-1)$ commensurate structure and tight-binding calculation for a (19,18) commensurate structure.

With the Hamiltonian Eq.(2.13) in $N \times N$ matrix form, it can be numerically diagonalized for each $\boldsymbol{k}$ in the first superlattice Brillouin zone ($N/4$ smaller than original graphene BZ). We used the model descibed in Ref.[18] to calculate for a (19,18) commensurate structure, which has a similar twist angle $\theta = 1.8°$ with the device we fabricated. The illustration of the MBZ and the calculated band structure is plotted in Fig. 2.4.

From the calculated band structure we can see that the massless Dirac fermions near zero energy are preserved, which is consistent with the continuum model as described in Section 2.2. They are doubly degenerated at each of K_s and K_s' of the MBZ. The Fermi velocity at the Dirac points is reduced to about 20 % of that of monolayer graphene.

Interestingly, a energy gap is opened at Γ_s between the two lowest-energy bands and the bands above them. This behavior is not predicted by the simplest form of the continuum model as we described[1]. Although it seems analogous to the new generation of Dirac points in graphene/h-BN heterostructure at low twist angles, the new Dirac points are located at M_s of the MBZ while this gap in TwBLG is located at Γ_s. They also have different degeneracy, *i.e.* the number of Fermi pockets. The vast difference between these two systems that look similar at a first glance can be systematically understood using a symmetry analysis.

2.4 Symmetry in TwBLG

The symmetry of a system can tell us what properties it *must* have or *must not* have. For example, Kramer's theorem requires that any system with time reversal symmetry (TRS) must have eigenstates in pairs that are related by $\boldsymbol{k} \rightleftharpoons -\boldsymbol{k}$ and spin up$\rightleftharpoons$down.

Twisted systems generally have less symmetry compared to their building layers because of the rotational mismatch. For instance the inversion symmetry is broken in both graphene/h-BN and TwBLG, because inversion requires layer exchange and twist angle reversion which cannot be compensated by any translation. Indeed a large energy gap has been observed at the Dirac point of graphene/h-BN because of this inversion symmetry breaking. However, as we see in the last section in TwBLG there is generally no such gap opening at the Dirac point. Therefore we conclude that some extra symmetries must be protecting it.

The commensurate structure $(n, n-1)$ as shown in Fig. 2.3(a) can be classified as belonging to $P321$ space group (# 150). It has a primary 3-fold out-of-plane rotation axis centered at the registered atoms and three two-fold rotation axes along $\boldsymbol{A}_1$, $\boldsymbol{A}_2$ and $\boldsymbol{A}_1 - \boldsymbol{A}_2$. There is no mirror symmetry or inversion symmetry in this lattice. Time reversal symmetry is indeed preserved at zero magnetic field because none of our analysis involved spin or magnetization.

---

[1] By taking into account more Fourier components of the inter-layer hopping amplitude this gap is be able to be described.

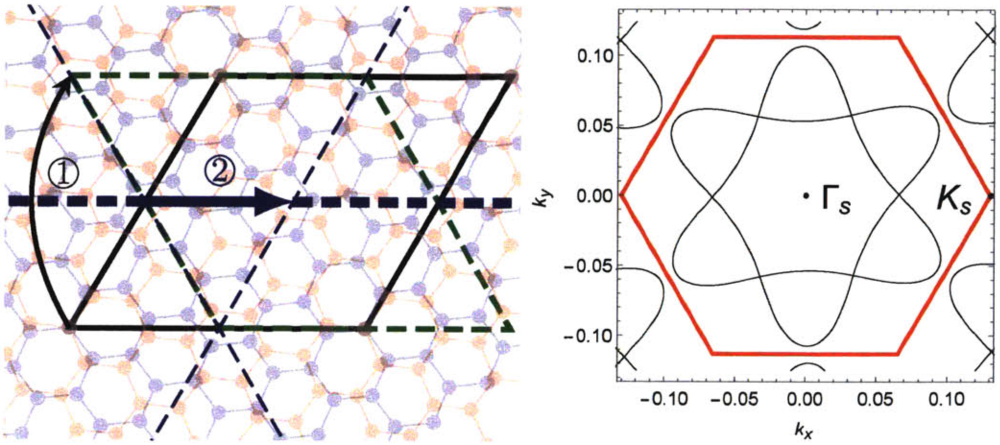

(a) Screw Axis (blue dashed lines)

(b) Fermi contour at $E = 0.035\,\mathrm{eV}$. Red hexagon is the MBZ

Figure 2.5: Extra symmetries in TwBLG

Although inversion symmetry does not exist in TwBLG, TRS and Kramer's theorem still has an effect on the band structure. A TRS transforms $\boldsymbol{k}$ into $-\boldsymbol{k}$, and therefore in Fig. 2.5(b) we see the Fermi contour is symmetric about $\boldsymbol{k} = 0$. In other words, the two large triangles are time reversal counterparts of each other. Combined with the three-fold rotational symmetry, we naturally have this hexagonal star shaped Fermi contour.

Chapter 3

Experiment Techniques

In this chapter, we describe the techniques that we utilize to fabricate TwBLG devices, and the setups that we use to measure the transport properties of these devices. One of the main reasons that some of the features we observed were not discovered before is that the range of twist angles that these phenomena happen is small, typically between 1∼2°. Therefore precise twist angle control is very important in this experiment. In Section 3.1.3 we describe a novel "tear & stack" technique that is independently developed and later reported in Ref.[21]. In Section 3.2 we will briefly introduce the standard setups for low-temperature magnetotransport measurements.

3.1 Sample Fabrication

3.1.1 Exfoliation

The traditional method of preparing graphene flakes is mechanical exfoliation[1]. This method is shown in Fig. 3.1(a). Natural graphite crystals are stuck on a piece of sticky tape. These crystals are repeatedly thinned out by blank tapes. The resulting tape is then transferred onto a silicon substrate. When the tape is removed, van der Waals force between the top layers of the graphite crystals and the substrate will drag down a portion of the crystals with thicknesses ranging from monolayers (0.34 nm) to hundreds of nanometers. The substrate is examined under a optical microscope to search for monolayer flakes, a process usually dubbed 'flake counting'. The size of the resulting monolayer flakes are usually on the order of 10 µm, but can be as large as 200 µm when the exfoliation is extraordinarily good.

Since the early days of graphene research, many other ways of preparing graphene

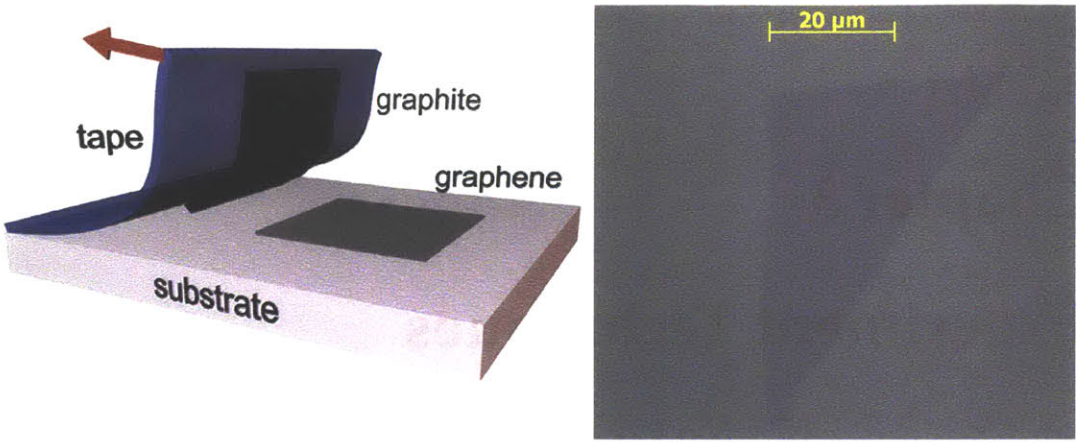

(a) Mechanical Exfoliation (b) Optical image of monolayer graphene

Figure 3.1: Exfoliation of graphene

have been developed. Most notably Chemical Vapor Deposition (CVD) can grow large scale continuous graphene sheets on the order of centimeters or even meters[22, 23]. However none of these methods to date are able to produce graphene flakes that have comparable electron mobility compared to those prepared by mechanical exfoliation.

H-BN flakes can be exfoliated in a similar way from crystals grown by our collaborators. In our experiment we use h-BN flakes that are 20~40 nm thick to act both as encapsulation layers and as gate dielectric.

3.1.2 Dry Transfer Technique

After exfoliation, the different flakes must be stacked in the correct order to make a complete device. This procedure is usually called *transferring*. Usually a transferring technique can be classified as either *wet* transfer or *dry* transfer depending on whether the flake is brought into touch with solvents or not during the transfer. Dry transfer has the advantage that the flakes are not contaminated by the solvent and thus the interface can be kept as clean as possible.

A reliable dry pickup/transfer technique with sticky polymer Poly(Bisphenol A carbonate) (PC) currently being used in our group was originally improved upon that described in Ref.[24]:

1. The top h-BN flake (thickness 20~40 nm) is picked up by a PC/PDMS stack

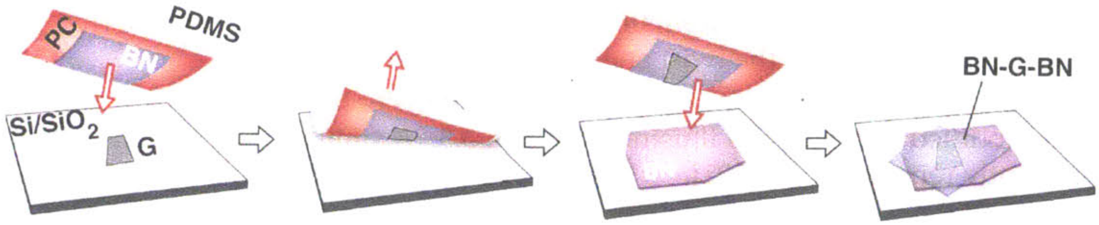

Figure 3.2: Illustration of dry transfer technique. Adapted from Ref.[24].

on a glass slide, which is mounted on a micro-manipulation stage. The pick-up temperature is usually at 90 °C.

2. The bottom surface of the h-BN flake can subsequently pick-up other flakes with van der Waals force. The pick-up temperature can be room temperature for monolayer graphene flakes, or up to 90 °C for thicker flakes such as graphite, TMD, or another thick h-BN flake.
3. After the stack is fully assembled, the sticky PC film is released onto a target substrate by heating up to 150 °C. The target is usually a bottom h-BN flake or gate electrodes made of graphite or metal.
4. The sticky PC film is removed by rinsing in chloroform for a few minutes.
5. The resulting stack is annealed in forming gas (Ar/H_2) for 2~3 h to remove polymer residue on the top surface.

It was shown that by putting graphene on top of a h-BN flake the electron mobility of graphene can be vastly enhanced [25]. By putting another layer of h-BN on top, we encapsulate the graphene flake from all external contaminations during later fabrication steps. Therefore all our devices fabricated so far are fully-encapsulated.

3.1.3 Tear&Stack Modification

Precise angle control plays a crucial role in the transport study of low angle TwBLG, because the change of the twist angle by a fraction of one degree can have dramatical difference on the electronic structure of TwBLG. Previously, the fabrication of low angle TwBLG is usually by luck: two pieces of graphene are picked and aligned with each other using their straight edges as precise as possible, and the resulting twist angle is distributed in a small range of say −2°∼2°. With this technique, we cannot possibly control the twist angle we want to study.

Therefore, a modification on the normal dry transfer technique was developed. This modified procedure is illustrated in Fig. 3.3. A similar process is also independently reported in Ref.[21].

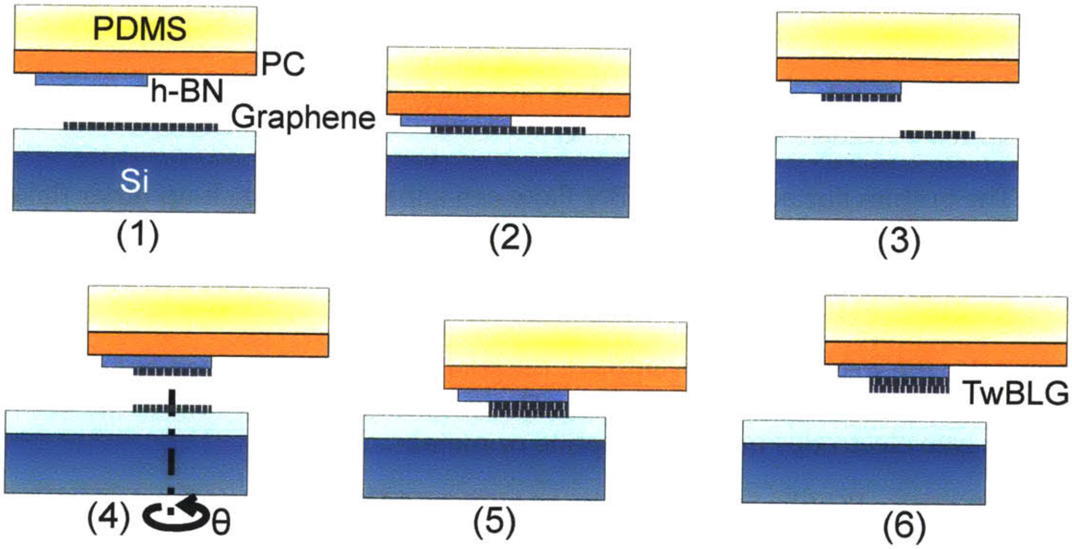

Figure 3.3: Modified dry transfer technique

Instead of using two pieces of graphene flakes to make a TwBLG, we use only one piece and tear it apart by the edge of a h-BN flake. The twist angle can be controlled by rotating the substrate after picking up the first half. Assuming the original flake is single crystal, the two halves have the same lattice orientation from the beginning and should thus be aligned when stacked together. In this way, we can control the twist angle to be precise to a fraction of a degree.

In reality, there are some difficulties that could lower the yield of this modified technique. Depending on the geometry and the direction of tearing, the graphene flake does not tear cleanly in some situations.

From previous trials it seems that heat annealing can change the twist angle after such a low angle TwBLG stack is made. Therefore we normally do not heat anneal the TwBLG samples after transferring and removing the PC film.

3.1.4 Patterning & Contacting

After transferring, the TwBLG is fully-encapsulated in two flakes of h-BN. We perform e-beam lithography (EBL) to define the geometry of the device, etch through the h-BN to expose the edges of the TwBLG, and evaporate the top gate.

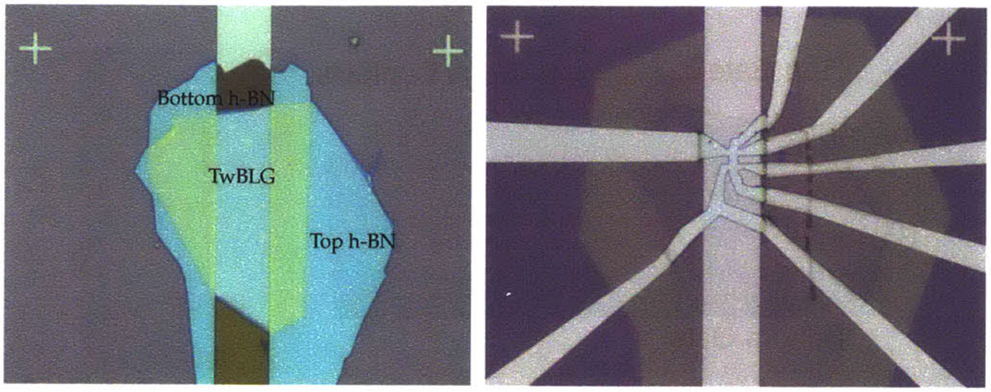

(a) Device before contacting (b) Device after contacting

Figure 3.4: Device before and after patterning & contacting.

Usually after transferring the TwBLG stack, a lot of bubbles will accumulate between the two h-BN flakes. One of the main tasks of patterning is to select the region that is free of bubbles or wrinkles, so that it is suitable for transport studies. There are mainly three patterning steps in our fabrication process.

1. Define the geometry of the top gate. We use PMMA as a liftoff mask, on which the top gate region is exposed with EBL to allow metal to be evaporated on top of the top h-BN flake.

2. Etch contacting the TwBLG using Reactive Ion Etching (RIE). As reported in Ref.[24], Au/Cr electrode evaporated on the 1-dimensional *edge* of graphene can make superb electrical contact to it. We first define the contact region with EBL on PMMA. The exposed area is then etched with RIE such that everything is etched through (removed from the substrate). Metal contacts are then immediately evaporated and lifted off with the same mask.

3. Define the geometry of the device by RIE. In most situations we make 6-probe Hall bar devices. Usually the top gate is already defined as a Hall bar shape

and itself can act as a etch mask. However there is always a gap region between the top gate and the contacts that we must protect from being etched. Therefore we expose a third PMMA mask which protects these regions. Everything else that is neither protected by the top gate nor the PMMA mask will be etched away by the subsequent RIE.

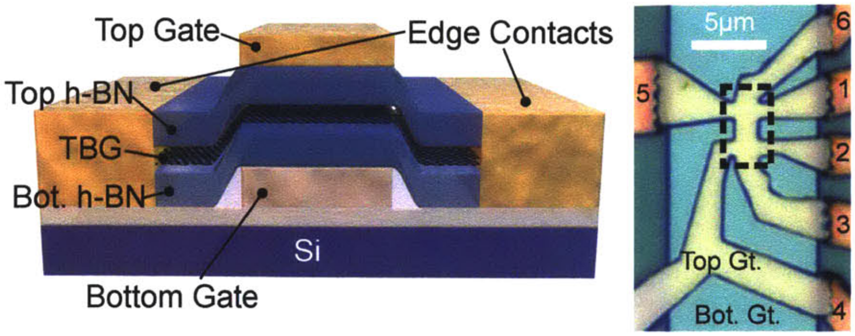

(a) Schematic (b) Device region

Figure 3.5: Schematic illustration of our TwBLG device.

Fig. 3.5 shows the structure of a finished device. With two gates we can independently control the total density on the bilayers and the inter-layer electric field. We do not use the silicon chip as a global back gate because it usually introduces charge puddles and lowers the electron mobility.

Usually the time required for fabricating a batch of 3~5 such devices from scratch is around 3 weeks. The size of device region is usually around 1×3 μm.

3.2 Measurement

Condense matter experiments tend to be carried out in cryogenic temperatures, from 4 K all the way down to 10 mK. This is mainly because the energy scale of most mesoscopic physics lies in milli-eV range, which can be easily washed out by thermal excitation.

3.2.1 Dilution Refrigerator

In our laboratory we have a dilution refrigerator that can go down to 40 mK and up to 12 T in magnetic field. Most of my experiments except the temperature de-

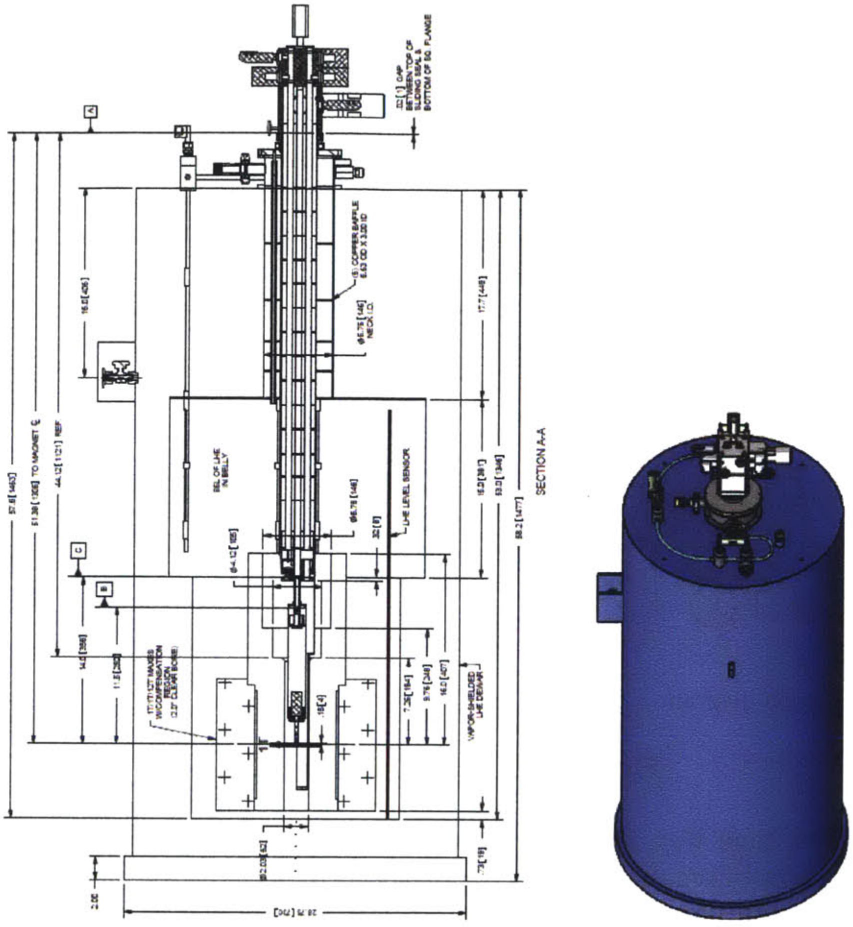

Figure 3.6: Structure of the dilution refrigerator

pendence were performed in this system.

3.2.2 Lock-in measurement

When measuring the conductivity or magnetoresistivity of a conductive sample, the bias voltage across the device is usually chosen to be small enough to make sure that Zener tunneling does not happen over any band gaps that we might be interested in. For our TwBLG samples we usually use $V_{\text{bias}} \sim 100\,\mu\text{V}$. This means that the current we measure will be on the order of nA.

Low-frequency lock-in measurements are widely used for measuring such small voltages or currents. The basic idea is to excite the sample with a reference frequency signal, and to measure only the amplitude of the same frequency. The output of a lock-in amplifier is the integral of the product of the output signal and the reference signal over multiple periods; any other frequency components will cancel out during this integration. Signal-to-noise ratio can thus be enhanced by a few order of magnitudes.

The circuit diagram of our typical measurements is shown in Fig. 3.7(a).

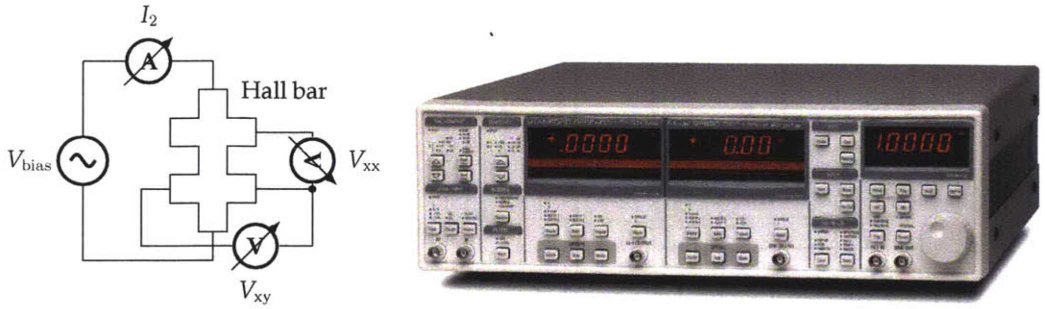

(a) Circuit diagram

(b) SR830 Lock-in amplifier

Figure 3.7: Lock-in measurement

The bias voltage V_{bias} is provided internally by the lock-in amplifier. We use three lock-in amplifiers that are synchronized with the same frequency to measure I_2, V_{xx} and V_{xy} simultaneously. The current I_2 is first converted to a voltage signal by a current amplifier.

In normal settings, $V_{\mathrm{bias}} = 100\,\mu\mathrm{V}_{\mathrm{rms}}$ and the lock-in frequency $f_{\mathrm{lock-in}} = 17 \sim 20\,\mathrm{Hz}$.

Chapter 4

Experiment Results and Discussions

In this chapter I will summarize the main experimental observations on the TwBLG devices, including the characterization using Atomic Force Microscopy (AFM) and Raman spectroscopy, and transport measurement data.

4.1 Atomic Force Microscopy

After transferring the stack and before patterning, we did AFM microscopy to examine the clean regions in the device. As can be seen in the AFM image Fig. 4.1, there are many bubbles sandwiched between the stack despite our effort to make it clean. However, we do find a clean region at the center of the sample that is free of any bubble or wrinkle, where we made our device.

4.2 Raman Spectroscopy

Raman spectroscopy is sensitive to the interaction of phonon modes between different carbon layers, and can therefore help us characterize the TwBLG[26].

Monolayer has a single strong Raman peak centered at around 2680 cm^{-1} (2D peak). According to Ref.[26] and our observation, TwBLG with *large* twist angle has a peak very similar in FWHM to monolayer peak except that the peak position is shifted to higher wavenumbers. On the other hand, low angle TwBLG behave more like Bernal-stacked bilayer graphene because of its modified band structure due to the strong inter-layer interactions. The FWHM is greatly widened and shoulder peaks appear in the spectrum. Therefore, from Raman spectrum we can easily judge whether a device has small twist angle or large twist angle.

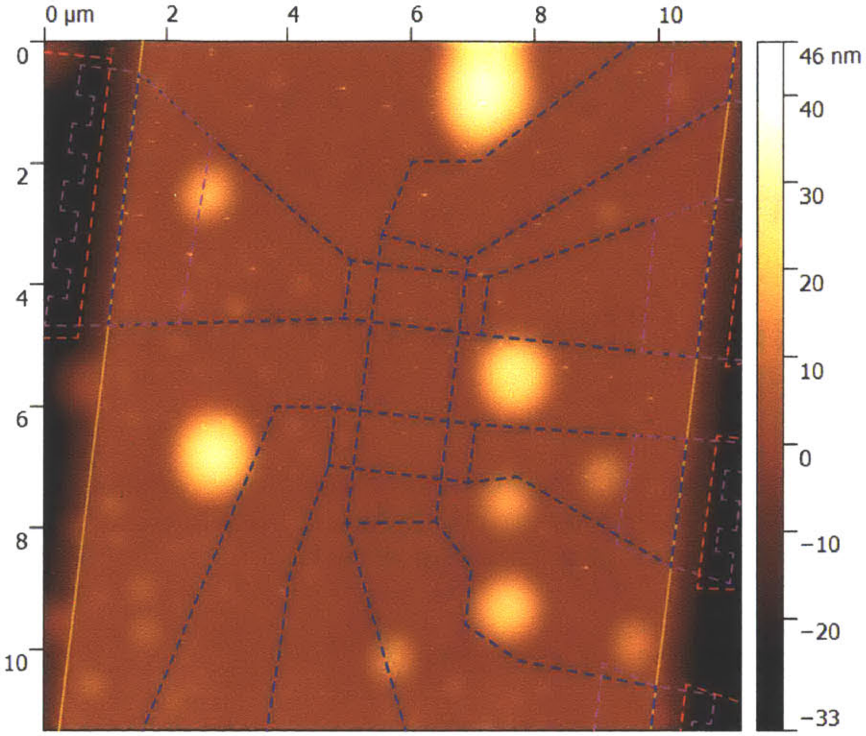

Figure 4.1: AFM image of the TwBLG device LT10-05. The dashed lines show the device region that was later fabricated on the sample.

Fig. 4.2 shows examples of the Raman spectrum near the 2D peak for three different samples. The monolayer (similarly for a large twist TwBLG) shows a very sharp and narrow Lorentzian peak, while the AB bilayer shows a wider peak with multiple shoulder peaks. The small angle TwBLG sample lies somewhat in between these two cases, as one would expect for it to be intermediate between a large twist TwBLG and an AB bilayer.

We cannot however accurately characterize the twist angle from Raman spectrum. The spectral resolution of the available Raman setup is not sufficient for a conclusive measurement.

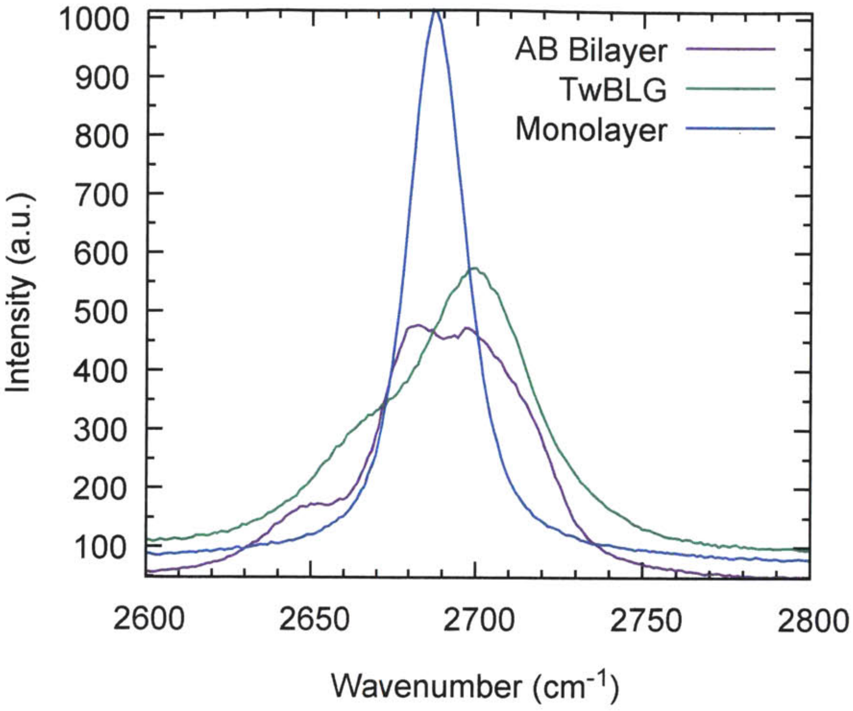

Figure 4.2: Raman spectrums of a Bernal AB-stacked bilayer graphene, a TwBLG and a monolayer graphene. Excited with 532 nm laser.

4.3 Insulating States & Temperature Dependence

By tuning the gate voltage on the two gates, we can directly control the total density on the bilayers,

$$n \approx \frac{C_{\mathrm{bg}}}{e} V_{\mathrm{bg}} + \frac{C_{\mathrm{tg}}}{e} V_{\mathrm{tg}}, \tag{4.1}$$

where C_{bg} and C_{tg} are the effective capacitance between the bottom/top gate to the TwBLG respectively. Fig. 4.3 shows the measured four-probe conductivity at different densities for two different TwBLG devices: S0 with large twist angle and S1 with twist angle smaller than 2°.

As can be seen from the measurement, both devices show approximately linear behavior near the charge neutrality point $n = 0$. These 'V'-shaped curves are characteristic of Dirac electron systems with linear dispersion near the Dirac point[1].

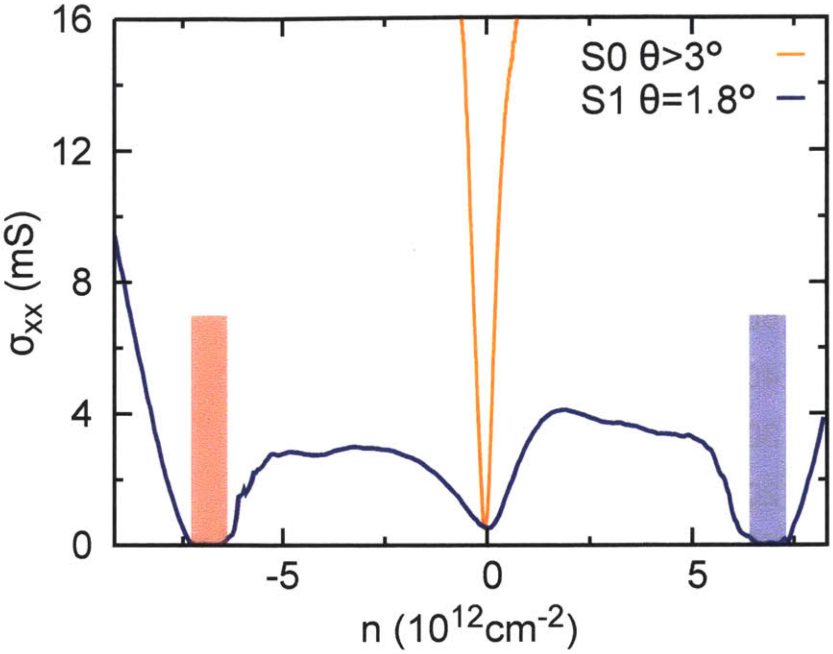

Figure 4.3: σ_{xx} measured at different total densities. The density is calculated from the applied gate voltages and estimated capacitances. Measurement done at 4 K.

The slope of each curve is determined by the field-effect mobility of the sample. We can thus estimate the field-effect mobilities of device S0 and S1 to be around 200 000 $\text{cm}^2\,\text{V}^{-1}\,\text{s}^{-1}$ and 20 000 $\text{cm}^2\,\text{V}^{-1}\,\text{s}^{-1}$ respectively.

While the conductivity of the device S0 increases monotonically and linearly with $|n|$ as one would expect for a simple Dirac system, the conductivity of the device S1 decreases after reaching a maximum and approaches zero near $|n|= 7.5 \times 10^{12}\,\text{cm}^{-2}$. These insulating states as we call them, occur symmetrically about the charge neutrality point and are thought to be associated with the superlattice band gaps as shown in Fig. 2.4.

From this density value, we can obtain the unit cell area of the superlattice to be

$$A_{\text{SL}} = 4/n_{\text{SL}} = 5.33 \times 10^{-13}\,\text{cm}^2 \tag{4.2}$$

Assuming each unit cell contains exactly one moiŕe (*i.e.* $(n, n-1)$ commensurate structure), $A_{\mathrm{SL}} = \frac{3a^2}{8\sin^2(\theta/2)}$. Therefore we have

$$\theta = 1.8^\circ \tag{4.3}$$

This value is in good agreement with our designed value, $\theta = 2^\circ$ during fabrication.

We also studied the size of the gap by performing temperature dependence measurements on the insulating states.

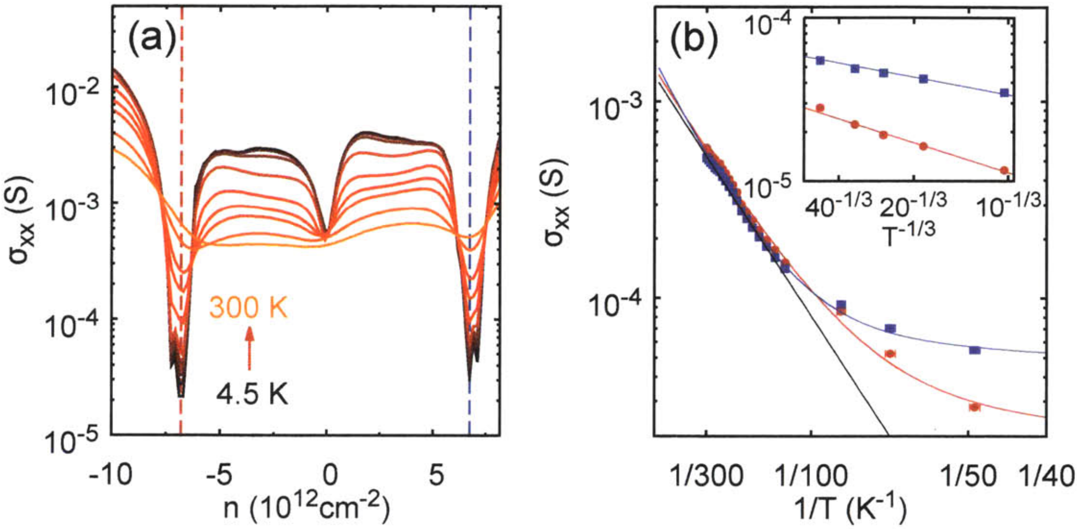

Figure 4.4: Temperature dependence of the insulating states in the TwBLG device with $\theta = 1.8^\circ$. (a) Conductivity as a function of carrier density and temperature. (b) Conductivity of the insulating states as extracted from the positions of the blue and red lines in (a), as a function of $1/T$. The inset is the low temperature part of the temperature dependence, plotted as a function of $T^{1/3}$.

At room temperature $T = 300\,\mathrm{K}$, the insulating states can still be identified as a faint dip in the conductivity curve. As temperature decreases, the conductivity decreases roughly exponentially with $1/T$, indicating an Arrhenius-type thermal activation behavior $\sigma = \sigma_0 \exp(-\Delta/2kT)$ where $\Delta \approx 50\,\mathrm{meV}$ is fitted from the slope of the $\log\sigma$–$1/T$ curve.

This large gap size is unexpected from existing theoretical literature, and is not reported by any other experiments to date.

At low temperatures (<100 K), the conduction deviates from the Arrhenius law significantly. We found out that the low temperature conductivity can be nicely fitted by a two-dimensional variable-range hopping term which can be expressed as

$$\sigma = \sigma_0 \exp\left[-\left(\frac{T_0}{T}\right)^{1/3}\right]. \tag{4.4}$$

4.4 Magnetotransport

We applied perpendicular magnetic field up to 11 T on the TwBLG sample to study its magnetoresistivity and Hall conductivity.

4.4.1 Hall Effect and Hall mobility

In an external magnetic field, the electrons in a two-dimensional system feel an in-plane Lorentz force and accumulate on one side of the device, resulting in a net Hall voltage that is perpendicular to the electric current flow. The ratio of the Hall voltage and the current is defined as the Hall resistivity

$$\rho_{xy} = \frac{V_{\mathrm{Hall}}}{I}. \tag{4.5}$$

From simple arguments of the Lorentz force it can be shown that

$$\rho_{xy} = \frac{B}{-ne}, \tag{4.6}$$

where n is the charge concentration, defined as positive for holes and negative for electrons. Therefore, from the sign of the Hall resistivity we can deduce the nature of the carriers in a condense-matter system.

The conductivity of a two-dimensional material is related to the carrier density by

$$\sigma = |n|e\mu, \tag{4.7}$$

where μ is the carrier mobility. Plugging this into Eq.(4.6), we obtain the formula for Hall mobility

$$\mu_{\mathrm{Hall}} = \frac{\sigma|\rho_{xy}|}{B}. \tag{4.8}$$

Fig. 4.5 shows the Hall resistivity and Hall mobility of the TwBLG device with twist angle $\theta = 1.8°$.

Near the charge neutrality point, the Hall resistivity follows the usual relationship $\rho_{xy} \sim n^{-1}$. As the density approaches the insulating states $n = \pm 7.5 \times 10^{12}$ cm^{-2},

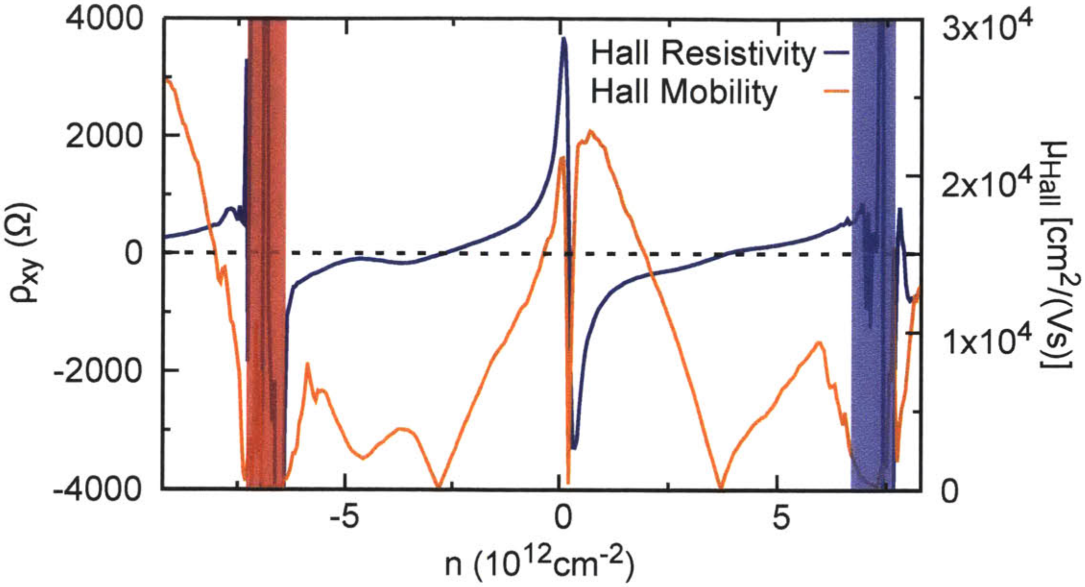

Figure 4.5: The Hall resistivity and mobility of the TwBLG device at different total carrier densities. Measured at 4 K.

however, the Hall resistivity switches sign, indicating the charge carriers has flipped their sign. This is consistent with the picture of a superlattice band structure, where as one approaches the superlattice band gap the electron-like orbits evolve into hole-like orbits. The Hall mobility as extracted from the low magnetic Hall effect according to Eq.(4.8) reaches $20\,000\,\mathrm{cm^2\,V^{-1}\,s^{-1}}$ near the charge neutrality point, which is consistent with the field-effect mobility and indicates a high sample quality in our TwBLG device.

4.4.2 Landau Levels and Degeneracy

At high magnetic fields, the Hall conductivity of a two-dimensional electron gas quantize to multiples of the unit quantum conductivity, $e^2/h \approx 25.8\,\mathrm{k\Omega}$. This phenomenon is known as the Quantum Hall Effect and is attributed to the formation of Landau levels in a magnetic field. When the chemical potential is located between the energy of extended states of two adjacent Landau levels, the bulk is insulating and the conduction is entirely due to the edge states associated with each filled Landau level. If we then measure the longitudinal magnetoresistivity and Hall resistivity, we obtain

$$\rho_{xx} = 0, \tag{4.9}$$

$$\rho_{xy} = \frac{h}{\nu e^2}. \tag{4.10}$$

The integer ν is usually called the *filling factor*. According to the tensor transformation between conductivity and resistivity, we also have

$$\sigma_{xx} = \frac{\rho_{xx}}{\rho_{xx}^2 + \rho_{xy}^2} = \begin{cases} 0, & \nu \neq 0 \\ \infty, & \nu = 0 \end{cases}, \tag{4.11}$$

$$\sigma_{xy} = \frac{\rho_{xy}}{\rho_{xx}^2 + \rho_{xy}^2} = \nu \frac{e^2}{h}. \tag{4.12}$$

Because of the degeneracy of electronic states in a system, usually ν cannot assume arbitrary integers but limited to a multiple of the degeneracy plus an integer shift which is provided by the Berry phase. In graphene, it is well known that the filling factor have a sequence of[1]

$$\nu = \pm 2, \pm 6, \pm 10, \ldots. \tag{4.13}$$

The 4-fold degeneracy is explained by the K, K' valley denegeracy and 2-fold spin degeneracy. The shift of 2 in the sequence is consistent with a Berry phase of $\pm\pi$ around two Dirac point of graphene respectively.

Fig. 4.6 shows color maps of ρ_{xx} and σ_{xy} versus the total density and the magnetic field. Minima in ρ_{xx} and plateaux in σ_{xy} correspond to fully filled Landau levels at the chemical potential. From the plateau values in σ_{xy} it is immediately obvious that near the charge neutrality point the filling factors have a sequence of

$$\nu = \pm 4, \pm 12, \pm 20, \ldots, \tag{4.14}$$

which is exactly twice that of the monolayer graphene sequence. This sequence is contradictory to the quantum Hall sequence of a Bernal-stacked bilayer graphene, which is $\pm 4, \pm 8, \ldots$[27], but can be understood if we consider it as two *separate* graphene layers. This hypothesis is supported by the low energy band structure of the TwBLG which does have a Dirac-like dispersion and an 8-fold degeneracy (see Chapter 2).

In an n–B plot or a 'Landau fan diagram', each Landau level follows a straight line that originates from the charge neutrality point and has a slope given by

$$B = \frac{\phi_0}{\nu} n, \tag{4.15}$$

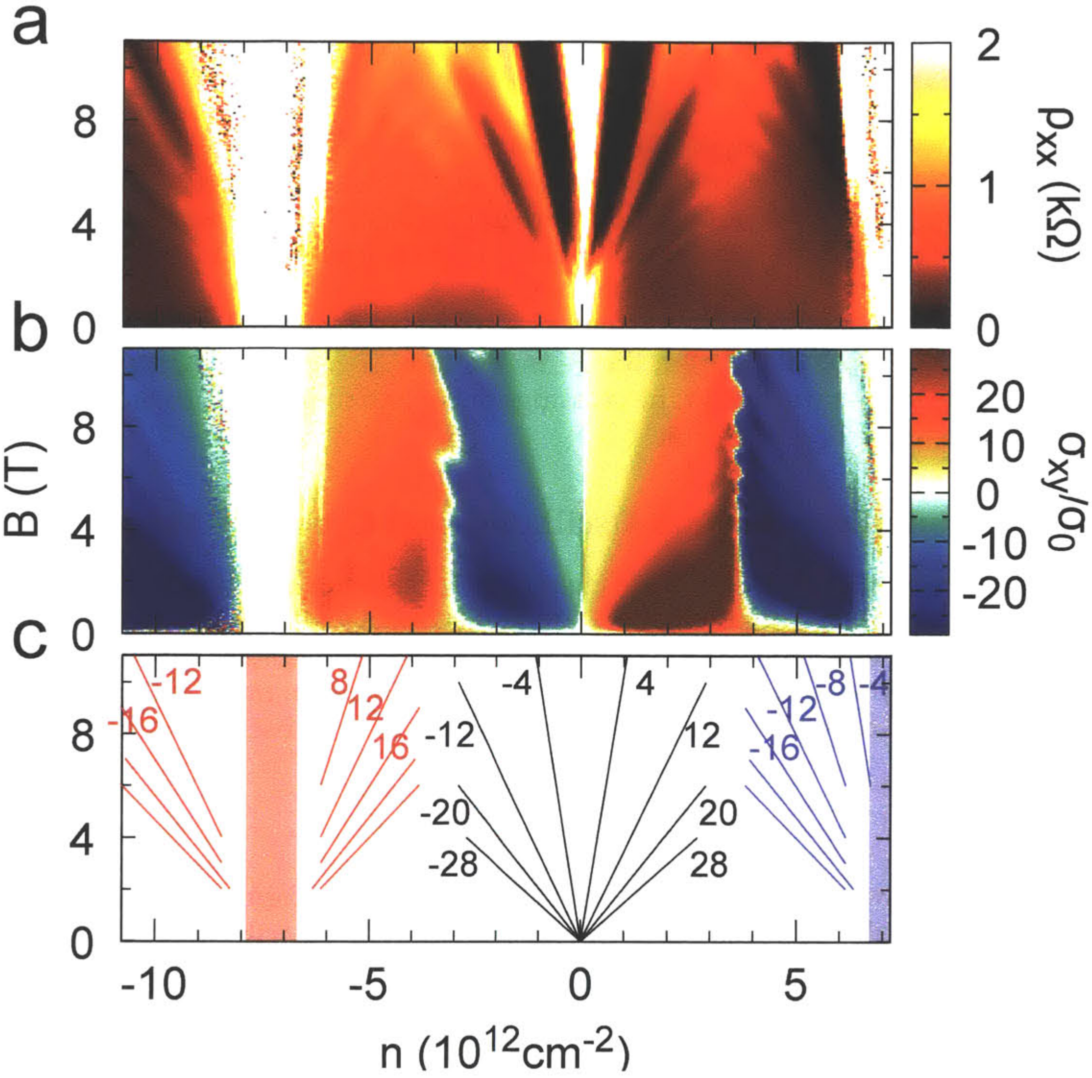

Figure 4.6: Quantum Hall Effect in TwBLG. Measured at 40 mK.

where $\phi_0 = h/e$ is the quantum unit flux and ν is the filling factor.

For a multi-band system, there can often be more than one Landau fan. Indeed near the insulating states, we find another two sets of 'satellite' Landau fans. This is another solid evidence that we do have band edges at these insulating states. From both the slope of the Landau fans and the σ_{xy} plateau values, we determine the filling factor sequence of the satellite fans to be

$$\nu = 0, \pm 4, \pm 8, \pm 12, \ldots . \tag{4.16}$$

There are two pieces of important information in this sequence: there is no Berry phase associated with the band edge; the Landau levels are 4-fold degenerate. The lack of Berry phase indicates that unlike in graphene/h-BN heterostructure where new generation of Dirac points occur when the first superlattice band is filled, here we most likely have a parabolic gapped system.

The 4-fold degeneracy is explained by the two-fold spin degeneracy and another two-fold degeneracy from the Fermi contour (Fig. 2.5(b)). An implication from this degeneracy is that at the crossings of the two triangular orbits, electrons *do not* jump to the opposite orbit.

4.4.3 Shubnikov-de Haas Oscillation and Cyclotron Mass

We also looked at the Shubnikov-de Haas (SdH) oscillation amplitude in ρ_{xx} at different temperatures. SdH oscillation can be viewed as a weaker version of quantum Hall effect at smaller magnetic fields. From the temperature dependence of the SdH oscillation amplitudes, we can extract the cyclotron mass of the material using Lifshitz-Kosevish formula, which states that the SdH oscillation amplitude

$$\Delta\rho_{xx} = A\frac{x}{\sinh(x)}, x = \frac{2\pi^2 kTm^*}{\hbar eB}. \tag{4.17}$$

Fig. 4.7 shows examples of the fit to Lifshitz-Kosevish formula. We find that the experimental data at low magnetic fields does fit nicely with the curve. Interestingly, at above about 5 T, a double frequency oscillation replaces the original oscillation at some gate voltages. Currently, we do not have a full understanding on this phenomenon. It is most likely due to the interference between the main Landau fan and the satellite fan at high magnetic fields, which could be seen as the onset of Hofstadter physics in the moiŕe superlattice.

Fig. 4.8 shows the SdH oscillation frequency (below 5 T) and the cyclotron mass at different densities. The peaks in SdH oscillation frequency plot are obtained by doing a Fourier transform on the ρ_{xx} versus $1/B$ for each gate voltage. The oscillation frequency B_F is directly proportional to the Fermi pocket area; in a single carrier system, we would expect B_F to follow a straight line

$$B_F = \frac{\phi_0}{N}|n|, \tag{4.18}$$

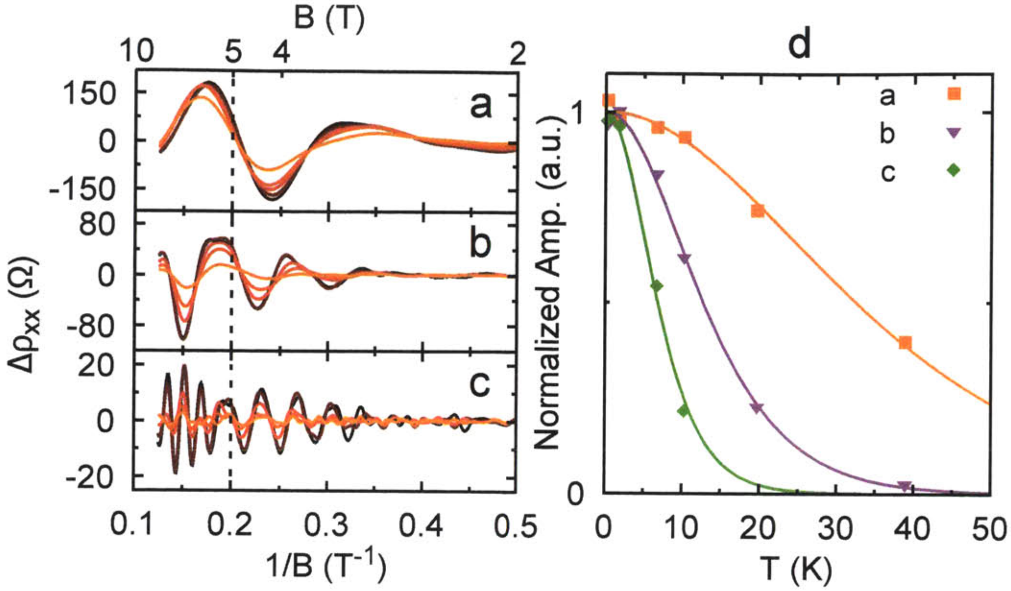

Figure 4.7: (a-c) SdH oscillation at three different gate voltages. (d) Fit of the temperature dependent SdH oscillation amplitude to Lifshitz-Kosevish formula.

where N is the degeneracy of the Fermi surface. In Fig. 4.8 we do see that the primary peaks are well fitted by the light blue curves, which are straight lines correspond to $N = 8$ near the charge neutrality point and $N = 4$ near the insulating states.

The cyclotron mass, on the other hand, is directly proportional to the density of states (DOS) per Fermi pocket in two-dimensional systems. They are related by

$$m^*(E) = \frac{h^2}{2\pi} D(E), D(E) = \frac{1}{N} \frac{dn}{dE}. \tag{4.19}$$

We already obtained the degeneracy N from the previous discussions; therefore we can directly compare m^* with the DOS that is obtained from tight-binding calculation, which is plotted as red dashed lines in Fig. 4.8(b). As can be seen, the experimental data and the theoretical data match reasonably well in shape. Unfortunately, the absolute value of these two differ by a factor of 2 consistently at all densities.

In summary, from the magnetotransport data we find that the tight-binding calculated band structure Fig. 2.4 can in general explain most features observed in the experiment. The absolute energy scale cannot be determined by the con-

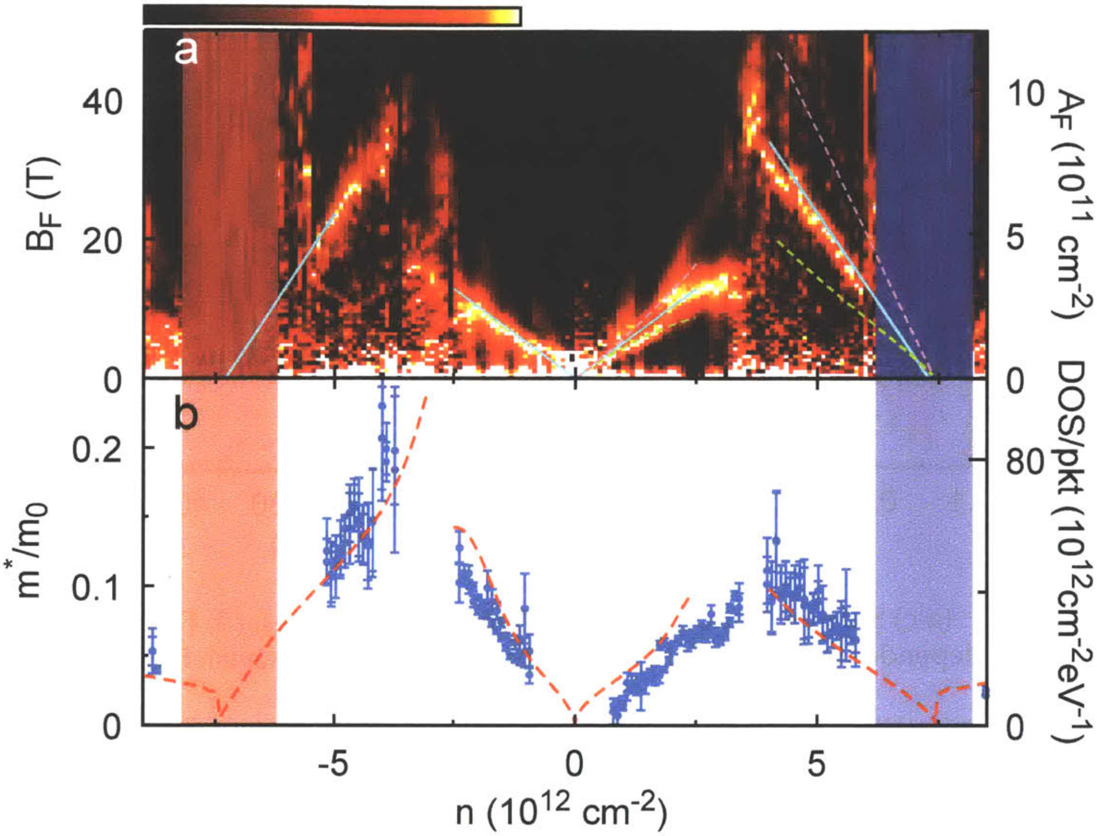

Figure 4.8: (a) SdH oscillation frequency. (b) Cyclotron mass extracted from Lifshitz-Kosevish formula and numerical calculated DOS per pocket.

ventional transport measurement. We think the factor of 2 discrepancy in DOS might be attributed to an underestimation of the bandwidth in the tight-binding calculated band structure.

4.5 Electric Field Dependence

Since all our devices are dual gated, we can independently adjust the density n and the interlayer electric field, which is in general proportional to a linear combination of the two gate voltages,

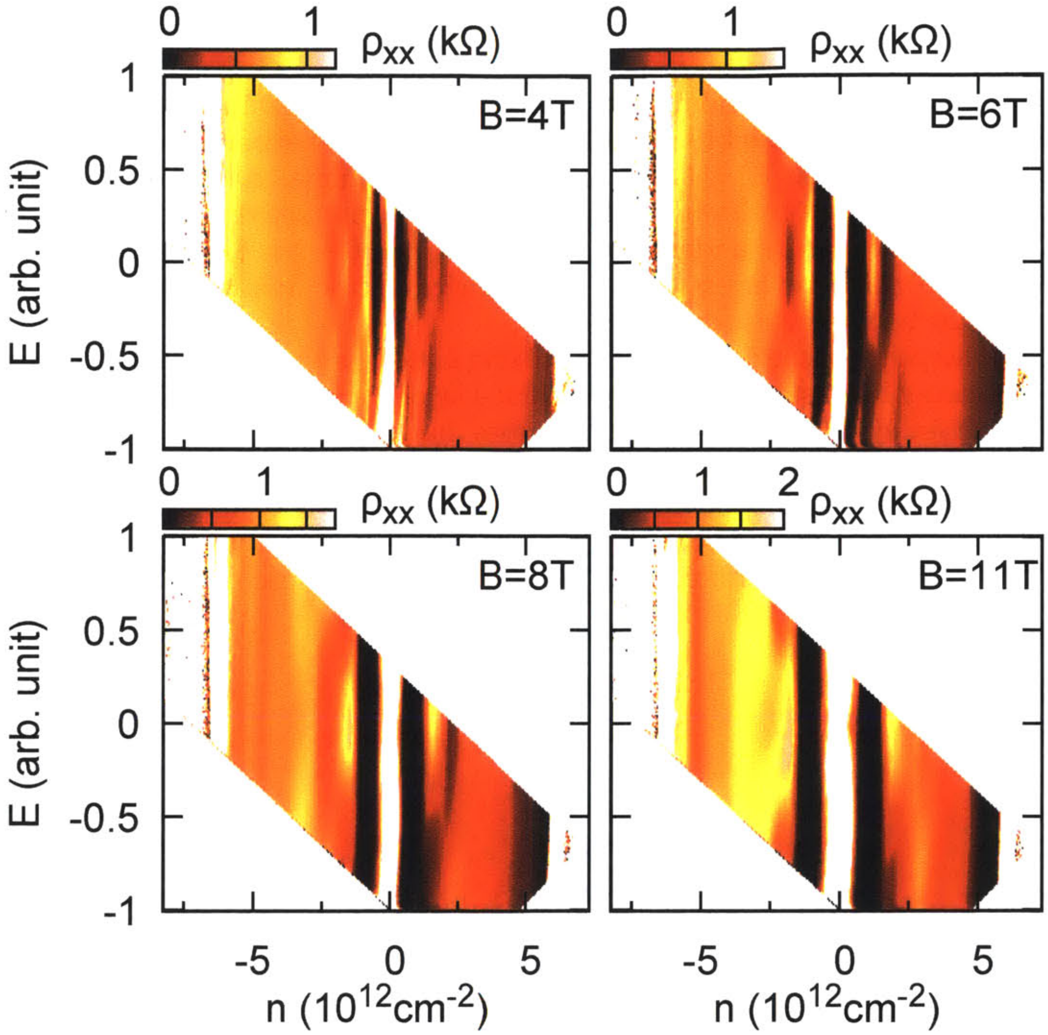

Figure 4.9: ρ_{xx} as a function of density and electric field, at four different magnetic fields. The cutoff of the map is due to limitations in gating the device.

$$E = aV_{\mathrm{tg}} - bV_{\mathrm{bg}}. \tag{4.20}$$

By applying differential gate voltages, we can increase the inter-layer electric field and unbalance the charge carrier densities as seen in top and bottom graphene layers in a TwBLG. The result is that the 2-fold layer degeneracy at the Dirac points are lifted and in a magnetic field a phenomenon called Landau level crossing will emerge[28].

We do observe this phenomena at low densities near the Dirac point. As seen in Fig. 4.9, the ρ_{xx} map exhibits a checkerboard pattern that expands with increasing magnetic field. At $E = 0$, we recover the ρ_{xx} minima corresponds to $\nu = \pm 4, \pm 12, \ldots$. However at $E \approx \pm 0.5$, the positions of the minima jump to $0, \pm 8, \pm 16$, *etc.* This sequence can be understood as $2 + (-2) = 0, 6 + 2 = 8, 10 + 6 = 16$, *etc.* from the two graphene layers, at finite inter-layer electric field where the filling factors in the two layers are different.

The emergence of the Landau level crossing pattern is an additional proof that the low-energy band structure retains a Dirac-like dispersion that can be tuned by the inter-layer electric field. At high densities, however, the Landau levels from the *satellite* fan does not change significantly from zero electric field to finite fields. This is also consistent with theoretical predictions: the band structure near the superlattice band edge does not respond to the inter-layer potential difference very much, since the inter-layer screening becomes strong at those densities and the potential difference has little effect.

Chapter 5

Summary

In this thesis research, we have experimentally studied the electronic properties of a new composite graphene system — twisted bilayer graphene (TwBLG). We fabricate numerous TwBLG devices using a modified dry transfer technique and standard lithography methods. The resulting devices are measured in cryogenic temperatures from zero magnetic field up to 11 T.

We have obtained definitive results that give us deeper understanding towards the physical properties of a two-dimensional superlattice, which was mostly studied in graphene/h-BN heterostructure before. Our results agree well with tight-binding predicted structures. The clearly visible insulating states and Landau level sequences indicate the existence of new band gaps that were never observed, which originate entirely from the effect of the moiŕe superlattice. Furthermore, the experiments are carried out at varying temperatures, which allows us to explore the size of the energy gap and the cyclotron mass of the band structure. The discrepancies between the experimental data and the theoretical predictions can provide insights for further theoretical studies.

The main results in this thesis are being prepared for publication.

Acknowledgments

First, I would like to thank my advisor Pablo Jarillo-Herrero for both his financial and intelligent support. This research cannot have been performed without his supervision.

Secondly, I should thank my colleagues Javier D. Sanchez-Yamagishi and Jason Y. Luo, who produced the very first preliminary results in low angle TwBLG (by accident!). They're my teachers of fabrication techniques. Many experiences from the previous failures that they told me proved extremely valuable in this research. Although Javier has left the group for his postdoc in the past year, he is still delightfully answering all my questions regarding TwBLG.

Valla Fatemi is a nice guy in my group since he loves to discuss with anyone about anything. In the data analysis stage of this research, he has provided many crucial suggestions on how to remove the background, how to increase the contrast of an image, *etc*, which was very useful for me. He and Liang Fu thought a lot about the symmetry of a TwBLG.

Shiang Fang is a theorist in Harvard University and collaborate with me for the tight-binding calculation using his *ab initio* model. He is a nice guy to discuss with and I would like to thank him for all the calculations he made.

I would also like to thank Yafang and Yaqing for providing help during the experiment. Finally, I should thank my parents for providing spiritual support from the other end of the Earth.

References

[1] K. S. Novoselov, A. K. Geim, *et. al. Nature* **438**, 197-200 (2005).

[2] A. K. Geim and I. V. Grigorieva. *Nature* **499**, 419–425 (2013).

[3] B. Hunt, J. D. Sanchez-Yamagishi, *et. al. Science* **340**, 1427-1430 (2013).

[4] C. R. Dean, L. Wang, *et. al. Nature* **497**, 598-602 (2013).

[5] J. D. Sanchez-Yamagishi, J. Y. Luo, *et. al.* arXiv:1602.06815 (2016).

[6] D. S. Lee, C. Riedl, *et. al. Phys. Rev. Lett.* **107**, 216602 (2011).

[7] H. Schmidt, J. C. Rode, *et. al. Nat. Comm.* **5**, 5742 (2014).

[8] J. M. B. Lopes dos Santos, N. M. R. Peres and A. H. Castro Neto. *Phys. Rev. Lett.* **99**, 256802 (2007).

[9] E. J. Mele. *Phys. Rev. B* **84**, 235439 (2011).

[10] G. Li, A. Luican, *et. al. Nat. Phys.* **6**, 109-113 (2010).

[11] A. Luican, G. Li, *et. al. Phys. Rev. Lett.* **106**, 126802 (2011).

[12] W. Yan, M. Liu, *et. al. Phys. Rev. Lett.* **109**, 126801 (2012).

[13] I. Brihuega, P. Mallet, *et. al. Phys. Rev. Lett.* **109**, 196802 (2012).

[14] T. Ohta, J. T. Robinson, *et. al. Phys. Rev. Lett.* **109**, 186807 (2012).

[15] K. S. Kim, A. L. Walter, *et. al. Nat. Mater.* **12**, 887-892 (2013).

[16] C-H Park, L. Yang, *et. al. Phys. Rev. Lett.* **101**, 126804 (2008).

[17] P. Moon, M. Koshino. *Phys. Rev. B* **85**, 195458 (2012).

[18] S. Fang, Efthimios Kaxiras. arXiv:1604.05371 (2016).

[19] P. R. Wallace. *Phys. Rev.* **71**, 622 (1947).

[20] R. de Gail, M. O. Goerbig, *et. al. Phys. Rev. B* **84**, 045436 (2011).

[21] K. Kim, M. Yankowitz, *et. al. Nano Lett.* **16** 1989-1995 (2016).

[22] X. Li, W. Cai, *et. al. Science* **324** 1312-1314 (2009).

[23] K. S. Kim, Y. Zhao, *et.al. Nature* **457** 706-710 (2009).

[24] L. Wang, I. Meric, *et. al. Science* **342** 614-617 (2013).

[25] C. R. Dean, A. F. Young, *et. al. Nat. Nanotech.* **5** 722-726 (2010).

[26] K. Kim, S. Coh, *et. al. Phys. Rev. Lett.* **108**, 246103 (2012).

[27] K. S. Novoselov, E. McCann, *et. al. Nat. Phys.* **2**, 177-180 (2006).

[28] J. D. Sanchez-Yamagishi, T. Taychatanapat, *et. al. Phys. Rev. Lett.* **108**, 076601 (2012).